

Adsorption, self-assembly and self-metalation of tetra-cyanophenyl porphyrins on semiconducting CoO(100) films*

Maximilian Ammon^a, Andreas Raabgrund^a, M. Alexander Schneider^{a,1}

^a*Solid State Physics, Friedrich-Alexander-Universität Erlangen-Nürnberg (FAU), Staudtstr. 7, 91058 Erlangen, Germany*

Abstract

The adsorption properties of free base 5,10,15,20-tetrakis(p-cyanophenyl)porphyrin (2H-TCNPP) on thin films of rock salt (rs) CoO(100) on Au(111) was studied in ultra-high vacuum (UHV) by a combination of low-temperature scanning tunneling microscopy and spectroscopy (STM/STS) and density functional theory (DFT). Films of rs-CoO(100) on Au(111) are prepared with excellent quality in a suitable thickness range. Particularly, we found that films of only 1 nm thickness show a semiconducting energy gap of $E_g = (2.5 \pm 0.2)$ eV. Upon deposition at 300 K, 2H-TCNPP adsorbs flat-lying and self-assembles in a long-range ordered superstructure that is stable at 80 K. The adsorption geometry of the molecules on the surface and within the self-assembly is analyzed by DFT. We find that the self-assemblies are stabilized by hydrogen bridge bonding via the functional cyano groups. Our STS data shows molecular states within the fundamental gap of the CoO. By comparison with the calculated DOS we determine the energetic positions of the frontier orbitals and find that the first three LUMO states 2H-TCNPP are located within the band gap, whereas the HOMO is shifted 1 eV below the CoO conduction band edge.

Upon annealing to 420 K the molecules change their appearance in STM images and a new prominent electronic state located at the center of the molecule is formed. We interpret this changed configuration as Co-TCNPP created by self-metalation on the oxide surface.

Keywords: porphyrin, cobalt oxide, self-assembly, self-metalation, electronic states, scanning tunneling microscopy

1. Introduction

The adsorption of porphyrins on solid surfaces are met with great interest due to their potential in surface functionalization and corresponding applications [1]. Most surface-science studies investigated porphyrins on (noble) metal surfaces illustrating the role of functional groups in the creation of self-assembly superstructures and also in (self-)metalation processes [2–4]. For applications in photo catalysis [5], photovoltaics [6], and others it is necessary to decouple the porphyrins from metal substrates either by (ultra-)thin insulating layers [7–10] or by using insulating or semiconducting substrates from the beginning [11–13]. To study the properties of molecules on bulk semiconducting

and insulating substrates is met with several problems, most notably that of anchoring the molecules for adsorption studies under clean ultra-high vacuum (UHV) conditions [14]. Therefore studies that address the adsorption geometry on bulk dielectrics in real-space by scanning-probe methods are still of limited numbers today [15–20].

An aspect related to the molecule-substrate interaction is whether or not metal atoms from the substrate can be coordinated by adsorbates. While porphyrin self-metalation (i.e. the coordination of a substrate atom in the porphyrin core) and the formation of metal-organic intermolecular bonds is quite common on metal surfaces [2], the fact that porphyrins may be metalated on oxide surfaces like MgO(100) [21, 22], TiO₂(110) [23], and CoO(100) and (111) [24, 25] is surprising. The origin of the metal atoms is ascribed to step edge rather than terrace sites.

*DOI: 10.1016/j.susc.2022.122044

¹alexander.schneider@fau.de

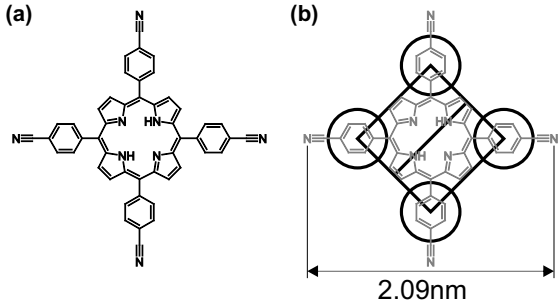


Figure 1: (a) Structure formula of 2H-TCNPP. (b) Schematic representation used to indicate the size and orientation of 2H-TCNPP in STM data. Note that the molecular axes are shown as the horizontal and vertical direction respectively, whereas the schematic representation indicates the nodal line in the STM appearance at 45° caused by the molecular pyrrole rings.

Here we investigate the adsorption properties and self-metalation of a functionalized free-base porphyrin on a semiconducting oxide surface by STM. We choose rock salt cobalt oxide in the (100) surface orientation (rs-CoO(100)) that by its semiconducting, antiferromagnetic nature is a very potent material for adsorption studies [25–30]. We grow films of high crystalline and of thickness larger than 1 nm on Au(111). As these films are not in the ultra-thin limit, they may be taken as representative of a bulk oxide surface.

2. Methods

2.1. Experimental

The experiments were performed in an ultra-high vacuum system, with two separate chambers for sample preparation and STM measurements. The base pressure in both chambers was below 1×10^{-10} mbar. For the preparation of the CoO film we used a thin stainless steel tube (“doser”) as oxygen inlet, which was positioned 2 cm in front of the surface to enhance the local oxygen pressure at the sample by a factor of 50 compared to back-filling the chamber [31]. All sample temperatures during the preparation were measured with a K-type thermocouple in direct thermal contact to the single crystal.

The Au(111) single crystal was cleaned by repetitive cycles of sputtering with Ne ions (1.5 kV) and annealing to 800 K. Cobalt was evaporated from an e-beam source, the cobalt atoms

flux was calibrated with a quartz microbalance and adjusted to 2.1×10^{13} atoms s^{-1} corresponding to 0.02 ML s^{-1} where 1 ML of rs-CoO(100) contains 1.1×10^{15} atoms cm^{-2} ($a_p = 3.01 \text{ \AA}$). A rs-CoO(100) film is formed via temperature-induced restructuring of a wurtzite CoO(000 $\bar{1}$) film as described in our previous publication [31] with an optimized procedure as follows. The initial cobalt oxide was grown reactively under oxygen atmosphere with an $p_{\text{O}_2} \approx 5 \times 10^{-7}$ mbar, while the surface was kept at 320 K rather than at room temperature, since it sped up the sample preparation time without any loss of quality regarding the rs-CoO(100) films. After the initial reactive growth the sample was annealed in UHV to convert the film from wurtzite cobalt oxide to rs-CoO(100). The exact conversion temperature depends on the film thickness and the growth conditions, so we monitored the conversion by simultaneous LEED measurements. For a nominal thickness of 4.4 ML rs-CoO(100) an annealing to 800 K was found to be optimal.

The 2H-TCNPP molecules (Figure 1) were evaporated from a home-built Knudsen cell evaporator held at a temperature of 650 K. The relation between evaporation time and molecular coverage was determined by evaporating onto clean Au(111) to yield approximately half areal coverage. Additionally, we tested the intactness of the molecules by reproducing 2H-TCNPP chains on Cu(111) [32], which would fail in case of missing CN end groups.

The homebuilt low-temperature STM was operated at 80 K for all measurements presented here. The bias voltage was applied to the sample, while the tip was virtually grounded via the I/V -converter. The scanning tunneling spectroscopy (STS) measurements were recorded with opened feedback loop using a lock-in technique ($V_{\text{rms}} = 20 \text{ mV}$, $f = 2.7 \text{ kHz}$). The spectra were normalized to the conductivity $G_{\text{sp}} = I_{\text{sp}}/V_{\text{sp}}$ prior to opening the feedback loop.

2.2. Computational

DFT calculations were performed using the the Vienna Ab initio Simulation Package (VASP) [33, 34] in the projector augmented wave (PAW) framework [35]. The generalized gradient approximation (GGA) of Perdew-Burke-Ernzerhof (PBE) [36] for the exchange-correlation functional was employed. The localized nature of the Co d -states was treated by the DFT+U approach of Dudarev with an effective $U_{\text{eff}} = (U - J) = 4 \text{ eV}$ [37] and $U_{\text{eff}} = 2 \text{ eV}$

for the Co atom in the Co-TCNPP molecule [38]. To account for van der Waals forces we used the Tkatchenko-Scheffler (TS) scheme [39]. The substrate was modeled by a four CoO layers thick, (100) oriented slab with 20 \AA vacuum between its repetitions along the [100] direction. 2H-TCNPP or Co-TCNPP was set on one of the slab surfaces, all molecular atoms and the top two CoO layers were allowed to relax, the two bottom CoO layers were kept at the bulk structure (with the appropriate DFT lattice parameter of $a_p = 2.97 \text{ \AA}$ as obtained from a corresponding bulk CoO calculation). The relaxation was done in a non-spin-polarized, Γ -point only calculation until forces were below 0.1 eV \AA^{-1} , the lateral dimensions of the slab were chosen according to the experimental unit cell (see below). To model electronic properties we used a four layer (8×8) rs-CoO(100) slab, carried out the relaxation as before and performed a spin-polarized DFT+U+TS self-consistent calculation converged to $\Delta E/E = 5 \cdot 10^{-6}$ taking into account the antiferromagnetic order of CoO. We ensured that the DFT+U approach ended in the lowest energy configuration for bulk CoO by choosing an arbitrarily high U_{eff} first and then reducing in steps until $U_{\text{eff}} = 4 \text{ eV}$. This procedure was repeated for the CoO slab with the adsorbed molecule.

3. Results and Discussion

3.1. Characterization of the substrate

The preparation recipe for the rs-CoO(100) films may be tuned to produce discontinuous films with large rs-CoO(100) patches and clean Au(111) areas side by side. For the present study such substrate preparations were used to allow for a direct comparison between adsorption of 2H-TCNPP on Au(111) and rs-CoO(100) and for the possibility of STM tip characterization and preparation for STS measurements. Therefore, films with a nominal thickness of 0.4 ML–4.4 ML were studied in detail in the following. The nominal thickness is a measure of the amount of cobalt in the CoO film expressed by the thickness of a hypothetical, homogeneous and closed film. Preparations with a nominal thickness of 1.0 ML–4.4 ML led to open rs-CoO(100) films, while e.g. for 5.7 ML completely closed rs-CoO(100) film was produced. Figure 2(a) depicts a LEED measurement of a nominally 1.9 ML thick oxide film, Figure 2(b) and (c) the corresponding STM

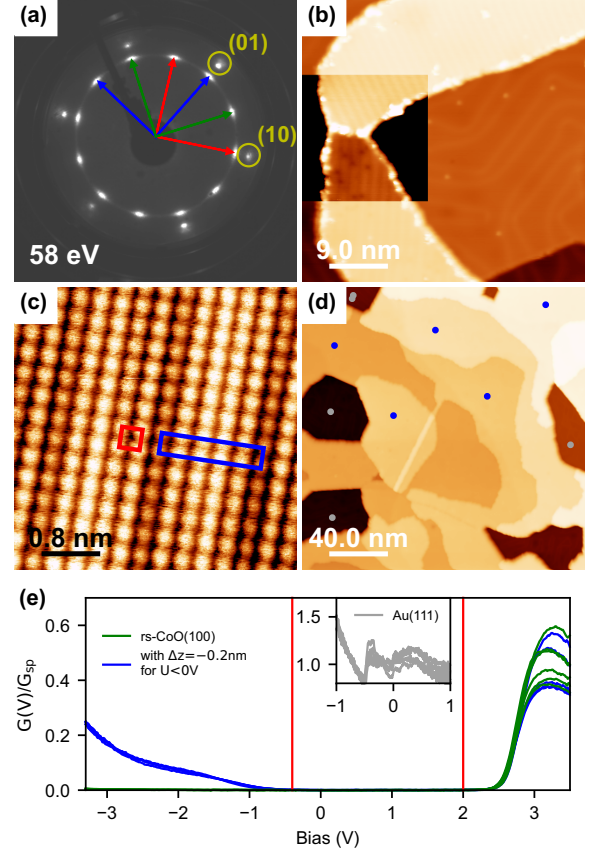


Figure 2: (a) LEED pattern of a nominally 1.9 ML thick rs-CoO(100) film. The Au(111) diffraction spots (yellow circles) are still visible. The reciprocal unit cells of the three rotational domains of the rs-CoO(100) film are marked with red, green and blue arrows. (b) The STM topography shows a flat film surface with a weak moiré pattern whose orientation and periodicity depends on the grain orientation to the surface. (c) Atomically resolved rs-CoO(100) surface showing a moiré that is locally reminiscent of a “ 5×1 ” with height variations of a few picometer. (red: primitive unit cell, blue: local moiré cell). (d) Overview STM image of a nominally 4.4 ML thick rs-CoO(100) film. The markers show the positions of the STS data depicted in (e). (e) Normalized differential conductivity curves showing a bandgap from -0.4 eV to 2.0 eV (red vertical lines). The tip was approached 2 \AA closer to the surface in the negative bias region enhancing the signal by a factor of ≈ 100 . Insert: spectra taken with the same tip on clean Au(111). STM parameters: (b) 1.0 V, 0.10 nA; (c) 0.3 V, 0.15 nA; (d) 3.0 V, 0.10 nA (e) prior to opening the FB loop defining G_{sp} : -3.5 V , 0.05 nA on rs-CoO(100) and -1.0 V , 0.4 nA on Au(111).

measurement. In contrast, Figure 2(d) shows an STM image of a nominally 4.4 ML thick film.

The ring of 12 diffraction spots in (a) corresponds to three rotational domains, as expected for the epitaxial growth of a rs(100) film on fcc(111). The diffraction spots of Au(111), including the moiré spots of the herringbone reconstruction, are still visible and indicate intact and clean Au(111) surface areas alongside the rs-CoO(100) islands. The comparison of the rs-CoO(100) and Au(111) spot positions allows to measure the lattice constant of the oxide film with great accuracy. We evaluated 18 independently prepared open oxide films with a nominal thickness from 0.4 ML to 4.4 ML and find a mean lattice constant of $a_p = (2.92 \pm 0.01) \text{ \AA}$ with no systematic dependence on the nominal film thickness in that range. We note, that thicker and closed films approach the bulk surface lattice parameter of $a_p = (3.01 \pm 0.01) \text{ \AA}$ [31]. STM measurements of the 1.9 ML films show that roughly 30%–50% of the surface is covered with oxide (see Figure 2(b)). The surface of the oxide film is atomically flat but shows a weak one-dimensional moiré pattern with a height variation below 10 pm (see area of enhanced contrast in Figure 2(b)). The moiré orientation and periodicity may differ from patch to patch which indicates some variations in the orientation of the oxide islands with respect to the substrate, in line with the radial smearing of the diffraction spots in the LEED pattern (see Figure 2(a)). In atomically resolved STM images the moiré appears most of the time as quasi “ 5×1 ” (Figure 2(c)). However, the fine details of the STM images reveal that this is only a local section of a much larger (maybe even incommensurate) unit cell ($2.92 \text{ \AA}/2.88 \text{ \AA} \approx 73/72$) in agreement with the LEED pattern. Therefore the oxide overlayer accommodates itself on the Au(111) similar to what has been found for the case of a single bilayer CoO(111) on Ir(100) [40].

Figure 2(d) shows a nominally 4.4 ML thick rs-CoO(100) film, that covers $(85 \pm 10) \%$ of the surface. The oxide film exhibits mono-atomic steps and terraces extending over several tens of nanometers, a situation similar to an ideal rs-CoO(100) surface. Since rs-CoO(100) is a semiconductor, the apparent height is bias dependent. We therefore used bias voltages $V_{\text{bias}} > 2 \text{ V}$ that allows tunneling into the conduction band and which should give a apparent height comparable to the geometric height. From images like Figure 2(d) the measured apparent height of the oxide surface with respect to the

clean Au(111) is $(1.2 \pm 0.3) \text{ nm}$ ($(5 \pm 1) \text{ ML}$). The areal coverage and deposited amount of Co is used to calculate the average film thickness, which results in $(1.4 \pm 0.2) \text{ nm}$ ($(5.2 \pm 0.6) \text{ ML}$) and compares well with the measured apparent height.

Figure 2(e) shows a series of STS measurements on large CoO terraces. The measurement positions are marked in Figure 2 (d). The tip quality was tracked by measuring reference spectra on Au(111) showing the fingerprint of the surface state (see Figure 2(e), inset). The rs-CoO(100) shows a semiconducting behavior with a wide bandgap, where $dI/dV(V)$ and $I(V)$ are zero. We observe a much stronger rise of the differential conductance at the conduction than at the valence band edge. To obtain suitable sensitivity the STS data of Figure 2(e) was taken for the negative and positive bias region separately whereby the tip was approached 0.2 nm closer to the surface at negative bias. From this kind of data we extracted more accurate values for the band onset by fitting the signal with exponential functions in the onset regions. Details of the fitting procedure can be found in Ref. [31]. The valence band onset is at $E_V = (-0.4 \pm 0.1) \text{ eV}$, the conduction band onset at $E_C = (2.0 \pm 0.2) \text{ eV}$ which leads to a measured bandgap of $E_g = (2.5 \pm 0.2) \text{ eV}$. This compares well to $E_g = (2.5 \pm 0.3) \text{ eV}$ found by a combination of photoemission and bremsstrahlung isochromat spectroscopy or optical spectroscopy [26, 27, 41]. An asymmetric position of E_F within the semiconducting gap was also observed by photoemission spectroscopy for w-CoO(100) films on Au [31] and CoO(100) films on Ir(100) [42] and therefore is presumably no artifact of the STS measurement.

3.2. 2H-TCNPP on rs-CoO(100): self-assembly

Figure 3 shows the result of the deposition of 2H-TCNPP at 300 K with submonolayer coverage on a nominally 4.4 ML thick rs-CoO(100) film. After cooling the sample to 80 K the molecules are found on the oxide as well as on the free metal. The great majority assembles into stable islands (Figure 3(b) and (c)). On the rs-CoO(100) surface, isolated 2H-TCNPP molecules are only found attached to step edges. This indicates that the molecules are mobile at RT or even below and that there are intermolecular forces stabilizing the assemblies. The apparent height of isolated molecules measured by STM at a bias voltage of 3.5 V yields $(0.25 \pm 0.04) \text{ nm}$ which can be taken as proof that the molecules are flat ly-

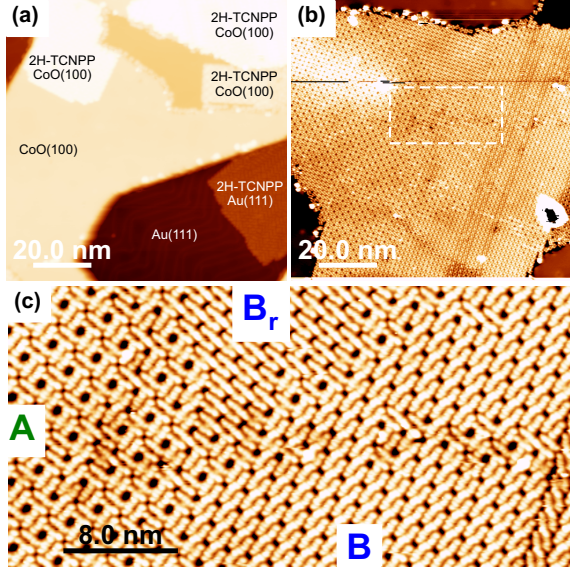


Figure 3: STM images taken at 80 K of submonolayer 2H-TCNPP deposited at 300 K on nominally 4.4 ML thick rs-CoO(100) on Au(111): (a) Clean Au(111), clean CoO(100) and compact islands of 2H-TCNPP on both areas are found. (b) Large scale self-assembly of 2H-TCNPP molecules on the rs-CoO(100) film. The area marked by the dashed rectangle is depicted in (c). (c) The self-assembly shows two distinct binding motifs, marked with *A* and *B*. Molecules in motif *A* are alternately rotated by 90° , while in motif *B* all molecules have the same orientation. Consequently the motif *A* shows a C_4 symmetry, while *B* is only C_2 symmetric and allows for domains B_r , rotated by 90° . STM parameters: (a) 3.5 V, 0.05 nA; (b) 3.0 V, 0.05 nA; (c) 2.5 V, 0.05 nA.

ing similar to findings of other porphyrins on oxide surfaces [21, 43–45].

However, the exact appearance of the molecule on the semiconducting substrate depends sensitively on the properties of the STM tip. This is demonstrated in Figure 4 where we compare images taken at exactly the same position, a domain boundary of both motifs, at different STM bias and tip conditions. The images of the left-hand column (a) and (c) represent the most robust tip state. Here the appearance depends very drastically on voltage as might be expected for a molecule on a semiconducting substrate in the spirit of the Tersoff-Hamann theory of STM [46]. Hence we term this tip as “metallic” (MT). The images of the right-hand column do not show a particularly strong bias dependence. In contrast, fine intramolecular details (like nodal structures) can be detected that are not visible in the left-hand MT images. This observation

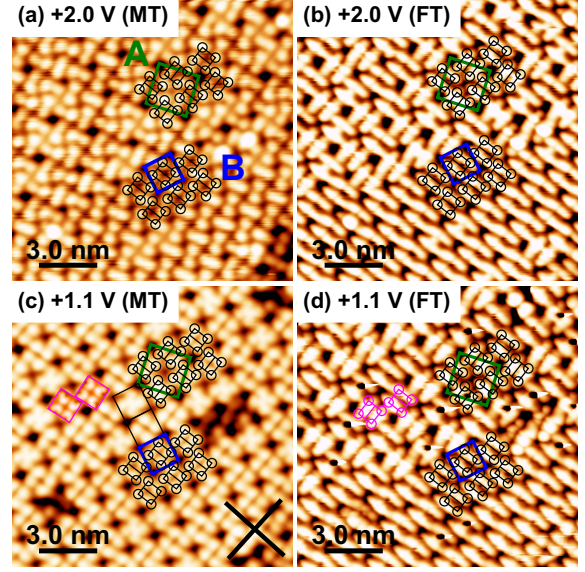


Figure 4: Self-assembly of 2H-TCNPP on CoO(100) after deposition on 300 K. The 2D self-assembly of 2H-TCNPP measured with a “metallic” and a “functionalized” tip (MT, FT) at two bias voltages. The position of identical molecules is indicated schematically in all four panels. (a) The STM contrast at 2.0 V with an MT tip mainly shows the four phenyl groups of the molecule whereas in (b) with an FT tip the molecular axis becomes more pronounced and the relative orientation between molecules in the two binding motifs *A* and *B* can be clearly distinguished. The cell of motif *A* (green cell) is a $(\sqrt{2} \times \sqrt{2})R45^\circ$ with respect to *B* (blue cell). (c) The measurement at 1.1 V with an MT tip is dominated by the molecular core as judged from the distance of the four maxima making up the molecule that are closer together than in (a). The majority of the molecules is imaged with a height minimum in the molecular center. The tiles with pink border are spin-averaged DFT+U STM image simulations corresponding to the molecules marked in panel (d). Measurement and simulation show a close to fourfold symmetry of the molecules at that bias. (Details see text.) The black cross in the lower right corner defines the [011] and $[0\bar{1}1]$ directions of the rs-CoO(100) substrate. (d) The “functional” imaging contrast is less bias dependent, hence the differences between (b) and (d) are minor. STM-Parameter: (a, b) 2.0 V, 0.05 nA; (c, d) 1.1 V, 0.05 nA.

together with the reduced stability of this imaging mode leads us to assign such images to “functionalized” tips (FT).

In the gas phase, the 2H-TCNPP molecule has C_2 symmetry due to the aminic ($-\text{NH}-$) and iminic ($=\text{N}-$) nitrogen atoms in the porphyrin macrocycle. On the surface, this symmetry manifests itself by a dark “central line” in the molecular STM images. The appearance of the molecule is very similar to that observed on metal surfaces, where it is

attributed to a saddle-shape conformation [47–50]. Hence the difference between assembly patterns A and B are simply different neighboring tautomers of 2H-TCNPP. These manifest themselves in the direction of the “central line” that is well defined in the FT contrast in Figure 4. We therefore use the contrast of the FT images to assign the correct orientation of the molecules. STM image simulations employing the spin-resolved DFT+U calculations shown as tiles in Figure 4(c) suggest that the orientation may only with great difficulties be inferred from the MT contrast images. However, this arrangement of the tautomers has consequences for the relative orientation of the cyanophenyl groups (see Section 3.5). The mechanism of the functionalization of the STM tip is unclear, the pick-up of a simple rest-gas molecule (H_2 , CO , O_2) seems likely [51, 52].

The square unit cells of the assemblies are indicated in Figure 4(a-d). Since there are uncovered rs-CoO(100) areas we may determine the underlying crystallographic directions of the substrate (Figure 4(c)). With respect to the rs-CoO(100) lattice we find that the cell is rotated by $\alpha = (20 \pm 4)^\circ$ and its lattice parameter is $a = (2.2 \pm 0.1)$ nm. The closest commensurate superstructure of the self-assembly of motif A is a $(\sqrt{58} \times \sqrt{58})R23.2^\circ$ -cell with $a = \sqrt{58} \times 0.292$ nm ≈ 2.2 nm that contains two 2H-TCNPP molecules (Figure 4(c)). The superstructure B is only half the size of that of A but the adsorption site of the molecules in both structures is the same, as proven by the continuation of the B unit cell into the area of motif A by the black squares in Figure 4(c). The appearance of this assembly is identical to that of 2H-TCNPP on two-bilayer rs-CoO(111) on Ir(100) [10]. Upon reinspection of that data we discovered that the lateral calibration of the STM was wrong by approximately 10% and therefore the size of unit cell was determined too large. As a consequence, the dipolar interaction between parallel cyano end groups proposed in [10] seems rather unlikely. See section 3.5 for a discussion of intermolecular forces stabilizing the self-assemblies.

3.3. 2H-TCNPP on rs-CoO(100): electronic properties

Within the assemblies we find three distinct molecular configurations after deposition of 2H-TCNPP on rs-CoO(100) at 300 K. In Figure 5 we analyze their electronic properties. Not surprisingly

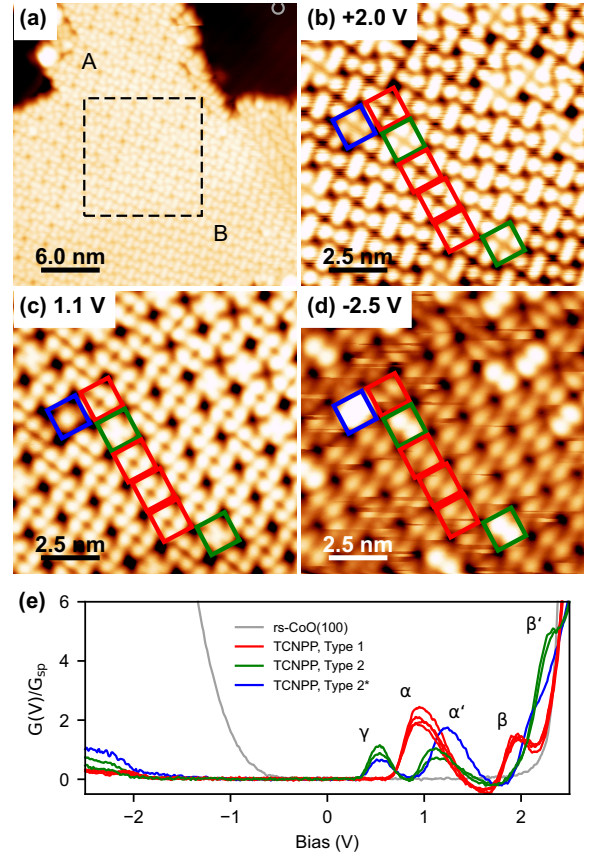


Figure 5: (a) Overview STM image of a 2H-TCNPP island with both binding motifs A and B. The dashed lines mark the area shown in panels (b-d). Three distinct molecular conformations can be discriminated from their appearance in (b)–(d): the majority configuration (red, type 1), a second (green, type 2) that is imaged as a projecting “cross” in (c), and a third configuration (blue, type 2*) that looks similar to the second configuration but is imaged as a spherical symmetric blob in (c) and (d). (d) The bone-shaped HOMO orbital shows the molecular orientation of the molecules. Normalized differential conductance STS spectra in (e) are taken with the tip positioned on the centers of the marked molecules in (b)–(d). For comparison, the spectrum on the bare rs-CoO(100) film taken with the same tip is shown also. STM parameters: (a) 2.0 V, 0.05 nA; (b) 2.0 V, 0.05 nA; (c) 1.1 V, 0.05 nA; (d) –2.5 V, 0.05 nA; (e) prior to opening the feed-back loop G_{sp} : 2.5 V, 0.4 nA.

we do not find any difference between molecules assembled in motif A or B.

The majority configuration (marked in red, Figure 5 (b)-(d)) shows the MT contrast discussed in the previous section and a “double cigar” contrast at large negative voltages. Its spectroscopic signature in the unoccupied states region ($V_{bias} >$

0 V) consists of prominent peaks α at $V_{\text{bias}} = (0.9 \pm 0.1)$ V and β at $V_{\text{bias}} = (2.0 \pm 0.1)$ V (Figure 5(e)). The cross-like (type 2) molecules (marked in green, Figure 5 (b)-(d)) show an additional peak γ at $V_{\text{bias}} = (0.6 \pm 0.1)$ V and the other two peaks shifted to higher energies. The previous α -peak (now α') is centered at $V_{\text{bias}} = (1.1 \pm 0.1)$ V and β' is shifted to higher energies and mingles with the conduction band onset above 2 V. Most striking the type 2 molecules are imaged clearly differently for negative voltages and can be discriminated against a third configuration (type 2*, marked in blue, Figure 5 (b)-(d)) that is imaged similarly at $V_{\text{bias}} = +2.0$ V but has its α' feature at (1.3 ± 0.1) V. Type 2/2* molecules have a dome-like appearance at voltages below α' , since only a state γ located at the core center contributes to the conductance. All molecular configurations show a very shallow increase of the differential conductivity for negative bias. Type 1 shows the weakest signal with an onset for the occupied orbitals at (-1.7 ± 0.3) V, the types 2 and especially 2* show stronger signals, so that the onset is clearer defined and results in (-1.8 ± 0.1) V for both. For all molecular configurations we find a substantial suppression of the STS signal from the valence band edge (gray curve in Figure 5(e)). This indicates the absence of molecular states in that energy region. As a consequence there is a very low tunneling transmission from valence band edge states due to the much larger distance between tip and CoO surface when probing a molecule.

3.4. 2H-TCNPP on *rs*-CoO(100): thermally induced self-metalation

The existence of different molecular configurations on the surface calls for an investigation of its reason. Possibilities that can be derived from literature are the occurrence of distinctly different porphyrin geometries, e.g. saddle-shape vs. dome-like [47, 48, 53, 54], or molecular reactions like the deprotonation [55] or metalation of molecules [3, 56].

From the appearance of the type 2 molecules with their filled center (at least visible at certain voltages), the metalation reaction is a possibility supported by the findings on metals [3, 4, 56]. The rate of a metalation reaction is expected to depend on temperature [57]. Metalation of porphyrins on cobalt oxide has also been observed before [58]. It is known (also established by our own experiments) that the 2H-TCNPP do not self-metalate on Au(111). Hence, the only possible candidate for the

outcome of a metalation reaction is Co-TCNPP for which Co atoms have to be provided by the oxide. In Figure 6(a) we show the situation after annealing to 420 K for 8 min. We observe that the remaining bare Au(111) surfaces are completely covered with molecules in an ordered self-assembly (Figure 6(b)). Only some molecules within the assemblies show spectroscopic and topographic signatures of a metalated porphyrin core, like the commonly observed protrusion in the center [3, 56], which arises from an additional state close to E_F [56, 59–61]. The ratio between empty and filled molecules on Au(111) varies from place to place, but metalated molecules were the minority species always. In contrast, our experiments with 2H-TCNPP on Au(111) indicate that with an appropriate (small) amount of Co atoms 2H-TCNPP molecules are metalated very efficiently at 420 K. Therefore, we conclude that the CoO does not produce a Co adatom gas on the bare Au(111) areas.

Conversely, most molecules remaining on the *rs*-CoO(100) surface show now the appearance of type 2 molecules. These molecules assemble predominantly into well ordered structures of motif A (Figure 6(c)). On some but not on all bare *rs*-CoO(100) surfaces we observe now defects that were not present after the preparation and deposition of 2H-TCNPP at 300 K (Figure 6(d)). Also some isolated molecules are found in these defective areas that are of an unknown configuration and were not observed before.

The analysis shown in Figure 7 also confirms the assignment with respect to the electronic fingerprint of the molecules. From our experiments we conclude that by annealing the 2H-TCNPP on *rs*-CoO(100) the dominant molecular species shifts from type 1 to type 2 molecules. Therefore we propose that type 2 molecules are in fact Co-TCNPP (see Section 3.5) the metalation process itself is activated at $T \geq 300$ K. By comparison with STM images of Co-tetraphenylporphyrin on Cu(111) [47], the appearance of type 2 molecules in our experiments could point to a relatively flat porphyrin macrocycle. The Co atoms most likely come from step edges, grain boundaries of the *rs*-CoO(100), or from the defects on some *rs*-CoO(100) terraces.

3.5. Density Functional Theory

The treatment of cobalt oxide by DFT is plagued with aspects that make the analysis of molecular adsorption on that material challenging. The correlation effects do not allow to reproduce the semi-

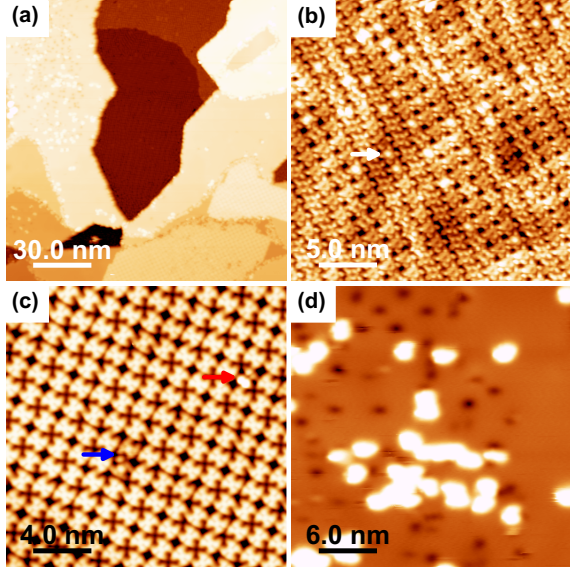


Figure 6: (a) Overview after annealing to 420 K. (b) 2H-TCNPP on the Au(111) area. The majority of Au(111) areas are completely filled with 2H-TCNPP molecules which suggests diffusion from the oxide to the metal substrate during annealing. Only few molecules have a filled core (e.g. white arrow) that are interpreted as Co-TCNPP. (c) The self-assembly 2H-TCNPP on rs-CoO(100) got more homogeneous, defects are healed out. Now most molecules are of type 2 (x-shaped, filled center). These are interpreted as Co-TCNPP molecules created by self-metalation on rs-CoO(100). The red arrow marks some exceptional type 1, the blue arrow marks two type 2* molecules. (d) Defect rich areas can be found on the rs-CoO(100) substrate. Only single molecules are adsorbed here. Such defects were not observed previously on the rs-CoO(100) substrate and could hence be the sites where part of the Co atoms for metalation originated. STM parameters: (a) 3.0 V, 0.05 nA; (b) 1.0 V, 0.05 nA; (c) 1.35 V, 0.05 nA; (d) 3.5 V, 0.05 nA.

conducting nature of the material without explicit considerations in the calculations. This calls for at least a DFT+U approximation. Furthermore, our work on wurtzite CoO [31] has shown that a plain DFT+U treatment would find the wurtzite polymorph energetically more favorable than the rock salt polymorph. This deficiency may be healed by inclusion of van der Waals corrections which are also required to account for the adsorption energy of large organic molecules. The omission of van der Waals corrections leads to arbitrary structural relaxations of the substrate slab with its large lateral unit cell that have nothing to do with the adsorption of the molecule. The antiferromagnetic coupling between ferromagnetic (111) planes has

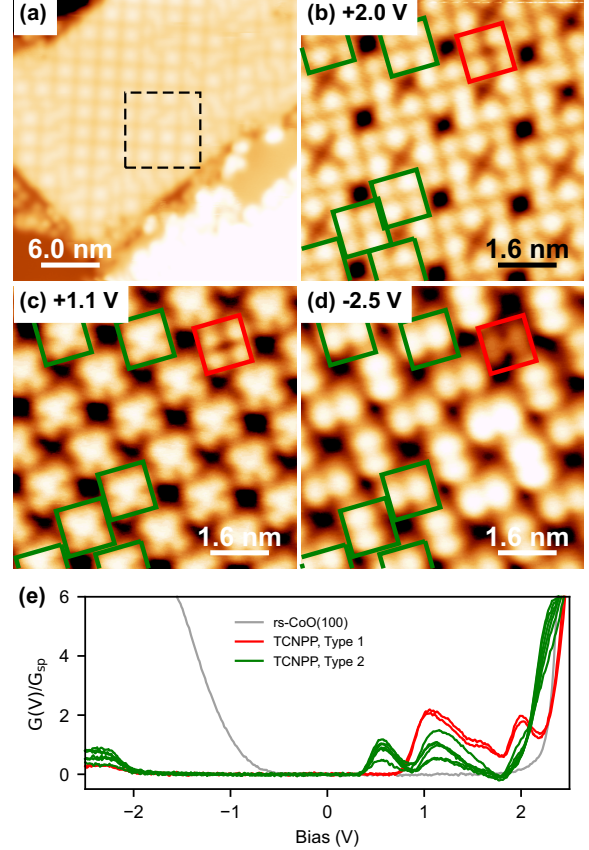


Figure 7: STM/STS measurement of molecules after annealing the sample to 420 K. (a) Overview of the area. The rs-CoO(100) reference is taken in the very lower left corner. (b-c) Bias-dependent topographies similar to Figure 5. Almost all molecules in this area are type 2 molecules (green). However, type 1 molecules are also found (red). (e) Normalized conductance STS data taken on the centers of the marked molecules proves the assignment. STM parameters: (a) 3.5 V, 0.05 nA; (b) 2.0 V, 0.05 nA; (c) 1.1 V, 0.05 nA; (d) -2.5 V, 0.05 nA; (e) prior to opening the feed-back loop G_{sp} : 2.5 V, 0.4 nA.

also to be taken into account to properly obtain a semiconducting rs-CoO(100) slab. Therefore a spin-polarized calculation must be performed using a correspondingly large unit cell of (8×8) to obtain electronic properties.

In this spirit, we discuss first the adsorption geometry and the occurrence of the two self-assembly motifs found in experiment. The structural findings of single adsorbed 2H-TCNPP are summarized in Figure 8(a) and (b). The adsorption site with the center of the molecule sitting on-top of a substrate O ion is energetically most favorable, as is

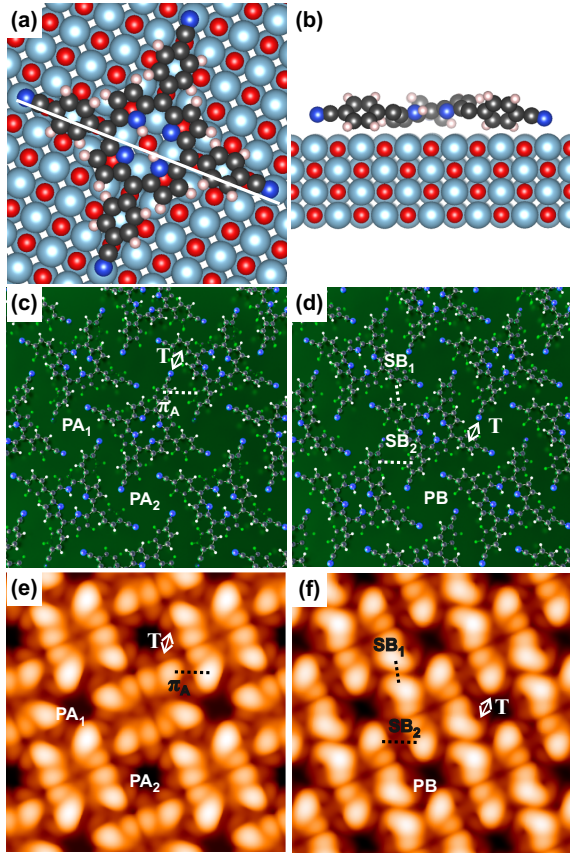


Figure 8: (a) Top view of the energetically most favorable configuration of 2H-TCNPP on rs-CoO(100). The geometry allows for a favorable interaction of the molecular N atoms with the Co ions of the substrate. (b) Side view, cut along the white line in (a). The molecule has the saddle shape configuration in which the iminic nitrogen atoms are pulled to the substrate. The cyanophenyl groups tend to be pulled parallel to the substrate but steric hindrance does not allow a perfectly flat geometry. The interaction between the CN group and the substrate comes apparent from the bending of the group towards the CoO in (b). (c) and (d): The resulting pore geometries PA₁, PA₂, and PB in the proposed assemblies A and B. A semi-transparent green plane was added to illustrate the orientation of the phenyl rings. Possible intermolecular interactions are labeled by T, π_A , SB₁, and SB₂. (e) and (f) corresponding empty-state DFT STM simulation of motif A and B. See main text for details about (c)-(f).

the strict alignment of the molecular axis along the [001] bulk direction of CoO. (For the definition of the molecular axes see Figure 1.) The molecule is found in a saddle-shape geometry where macrocycle pyrrole rings turn outward by 17.8°, while the deprotonated pyrrole rings turn inwards by 19.3° with respect to the surface normal. We find the

plane of the phenyl rings to be at 36° angle with respect to the surface normal. A slight bending of the terminal -CN group resulting in a calculated N-Co distance of (3.0 ± 0.1) Å indicates an attractive interaction with the substrate.

In Figure 8(c, d) we analyze the orientation of the phenyl rings in motifs A and B employing the non-spinresolved DFT calculations in a $(\sqrt{58} \times \sqrt{58})R23.2^\circ$ slab (notation with respect to the CoO(100)-(1 × 1) unit cell). In motif A two pore geometries (PA₁, PA₂), a T-type, and a π -stacking interaction configuration (π_A) exist (see Figure 8(c)). At PA₁ all surrounding phenyl rings points upwards like a roof surrounding the pore center. At PA₂ all groups are pointing downwards forming a square cone. This allows all phenyl ring pairs of neighboring molecules to be aligned in π - π stacking geometry (π_A). However, the distance between the phenyl rings (≈ 6 Å) is too large for any bonding relevance. In the DFT STM simulations the pore PA₁ appears as the cross-like pore and PA₂ as the square pore (Figure 8(e)). The simulation of how the pores are imaged matches nicely with the experimental results (Figure 4(a, c) and Figure 5(a, c)). Concerning the imaging mode of the molecules themselves, a close match is not expected since the non-spinresolved calculations result in a metallic and not a semiconducting CoO substrate.

In motif B, all pores have the same geometry (PB) with two rings on the opposite sides of the pore pointing upwards and two downwards (Figure 8(d)). As a consequence the phenyl rings cannot achieve a π -stacking configuration as the top edges of phenyl rings of two neighboring molecules point either towards (SB₁) or away from each other (SB₂). The modulation of this phenyl orientation is well visible in the experimental data for 2 V (compare Figure 4(a) or Figure 5(a)). SB₁ smears almost out to one single protrusion while at the place of SB₂ two separate protrusions are visible. The two upwards and downwards pointing groups of pore PB create a symmetry axis which is clearly visible in simulation and experiment as a dark line.

In the self-assemblies CN-groups are oriented at 90° angle to the axis of the cyanophenyl ring of a neighboring molecule, as observed on other substrates before [10, 32, 62, 63]. For the stabilization of the supramolecular assembly via the CN-groups [64] hydrogen bonding to the pyrrole group [62] or the phenyl rings [32] has to be considered. From our DFT-optimized structure of the assemblies we

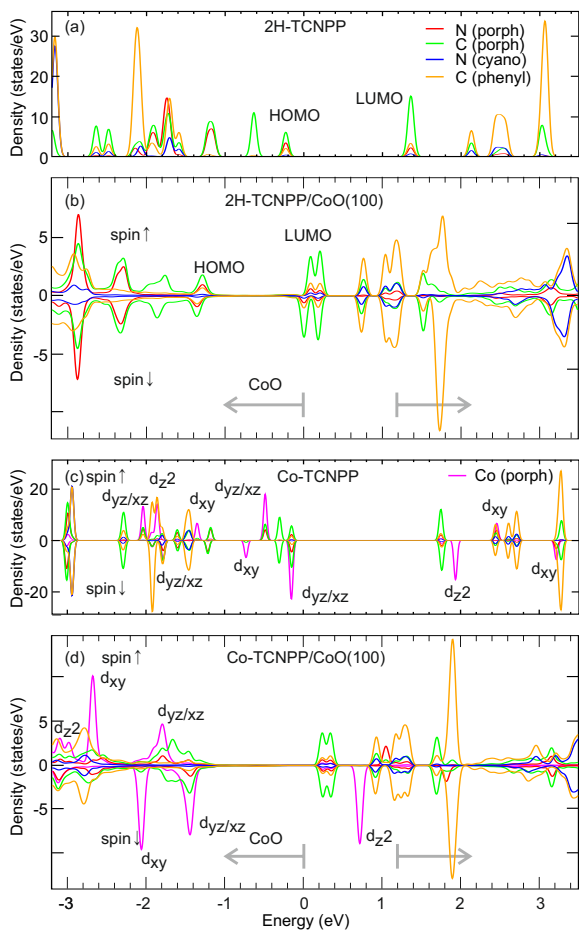


Figure 9: Calculated density of states (DOS) projected onto the N and C atoms of the molecular macrocycle (“porph”) and of the phenyl groups (“phenyl” / “cyano”) respectively. (a) DOS of 2H-TCNPP in vacuum. (b) Spin-resolved DOS of 2H-TCNPP adsorbed on rs-CoO(100). The calculated valence and conduction band regions of rs-CoO(100) are indicated by gray arrows. (c) Spin-resolved DOS of Co-TCNPP in vacuum and (d) adsorbed on CoO, additionally showing the DOS projected onto the coordinated Co atom of the molecule. Co-DOS is labeled by the orbital character of the d-states. For the Co atom in the molecule $U_{\text{eff}} = 2\text{ eV}$, for the Co in the CoO $U_{\text{eff}} = 4\text{ eV}$ was chosen (see text). The x-axis is the same for all panels, its origin is the energy of the highest occupied state of the respective calculation.

suggest that the bond to the pyrrole entity (-NH-containing, flat-lying) is dominating, we find an average bond distance of 2.8 and 2.6 Å for assemblies A and B respectively. In contrast, the CN...HC distance to a hydrogen of the phenyl ring of a neighboring molecule is at least 3.0 Å. This is still in a plausible range for hydrogen binding but the interaction is weaker.

In Figure 9 we summarize the calculated electronic properties of 2H-TCNPP and Co-TCNPP in vacuum and on rs-CoO(100) using spin-polarized PBE+U+TS. This procedure maintained the semi-conducting nature of CoO with a calculated band gap of 1.2 eV. We project the DOS to characteristic groups of atoms of the molecule which allows us to follow the shift of electronic states upon adsorption. We notice that the HOMO-LUMO gap of 2H-TCNPP in vacuum appears between states dominantly located at the porphyrin core (Figure 9(a)). The characteristic pattern of HOMO, HOMO-1 and LUMO, LUMO+1 (and following states) can also be recognized in case of 2H-TCNPP on rs-CoO(100) (Figure 9(b)). The LUMO orbitals shift down in energy, LUMO(+0) gets slightly filled whereas LUMO+1 and LUMO+2 remain in the gap at the conduction band edge of CoO. The HOMO states also shift down, the HOMO-LUMO separation remains approximately the same as for the free molecule.

The DOS of the Co-TCNPP was calculated using $U_{\text{eff}} = 2\text{ eV}$ vs. $U_{\text{eff}} = 4\text{ eV}$ for the CoO as motivated by [38]. The consequence of a smaller U_{eff} value is that the Co d-states move closer to the Fermi level. Obviously, CoO bandgap and molecular Co d-level positions depend sensitively on the choice of the DFT approximation which limits the meaningfulness of the comparison to experimental findings somewhat. Nonetheless, we propose the following conclusions. The calculations do not indicate significant electron transfer between molecule and substrate, hence the experimental α - and β -peaks in the band gap should correspond to the lowest lying LUMO states. The main difference between experimental spectra of 2H-TCNPP and Co-TCNPP adsorbed on CoO in the energy ranged probed can be explained by the appearance of an unoccupied, d_{z^2} derived Co state, which is also responsible for the “filled” molecular center in the STM images.

The calculations also support the view that the HOMO orbital should be located well below the valence band onset. The experimental spectra of 2H-TCNPP on CoO(100) of Figure 5(e) seem to suggest the absence of any molecular states in an energy range exceeding 3 eV which seems too large to be identified with the HOMO-LUMO gap of the adsorbed molecule. We therefore propose that the α -peak in Figure 5(e) should not be identified with a LUMO+0 state. We think it is composed of the states LUMO+1 to LUMO+3 and β partially of

LUMO+3 and of following states, as LUMO+3 is most likely already affected by hybridization with states at the conduction band minimum. Using the spin-resolved electron density to calculate a spin-averaged STM image of 2H-TCNPP, we notice that the clear characteristic “four-bump appearance” observed in experiment at a bias voltage of 1.1 V (i.e. beyond the α -peak) only starts to appear after charge density integration beyond the LUMO+2 slightly below 1.4 eV but is more clearly developed when the LUMO+3 is included, the corresponding STM simulation is shown in Figure 4(c). This indicates that α contains at least contributions from LUMO+1 and LUMO+2.

However, if the LUMO+0 state were to be included into the α -peak, it would have to be strongly modified by hybridization with the substrate (within the fundamental gap of CoO) to reduce the energetic distance to the LUMO+1 and following states for which there is no apparent reason. Similarly the appearance of the unoccupied Co d_{z^2} state γ energetically just below the state α (Figure 5(e)), is more consistent with a scenario where α does not contain the LUMO+0 state. Experimentally, a state expected at or near the Fermi energy ($V_{\text{bias}} = 0$ V) within the fundamental gap of an (undoped) semiconductor may not be available as transport channel due to its midgap position and hence can potentially not be detected in a tunneling experiment. The clarification of this needs a much more rigorous theoretical treatment of this complex system.

4. Conclusions

By careful tuning of preparation parameters we demonstrated the growth of rs-CoO(100) films on Au(111) suitable for adsorption studies. Films prepared with thicknesses of three to five CoO layers have the advantage that their electronic properties are close to bulk-like with a band gap determined by STS of $E_g = (2.5 \pm 0.2)$ eV. In that thickness range clean Au(111) areas are left that serve as a reference for calibrating STM tip properties. The rs-CoO(100) films may serve as a more reactive, easier to prepare, and structurally more perfect alternative to MgO [65–67] or NaCl films to decouple molecules from a metal surface [68–70]. Furthermore, due to the smaller band gap even thicker, homogeneous bulk-like oxide films can be prepared, suitable for a large range of surface-science techniques.

As an example, the adsorption, self-assembly, self-metalation and electronic properties of submonolayer 2H-TCNPP on rs-CoO(100) were studied. By a combination of STM and DFT analysis, we find that the molecules adsorb flat-lying, in a saddle-shape conformation, with their nitrogen atoms interacting weakly with underlying Co ions. When deposited at 300 K the 2H-TCNPP molecules assemble into two different, and hence energetically close or degenerate superstructures. The appearance of the superstructure in STM agrees well with DFT simulated images. From DFT structural relaxations we suggest that the self-assembly is stabilized by hydrogen bridge bonds between the nitrile terminal groups of 2H-TCNPP and hydrogen atoms from the molecular porphyrin core. By STS different configurations of the molecules are identified. One of them which is the majority species when the molecules are adsorbed at 300 K is assigned to 2H-TCNPP. A second configuration becomes dominant when annealing the system to 420 K. From the appearance of the molecules in STM, we propose that a self-metalation reaction has taken place and that the second species is Co-TCNPP. DFT calculations of the electronic density of states support this view and tentatively allow to identify the features of the STS measurements. It is found that upon adsorption the molecular states shift down in energy to an extent that the HOMO-LUMO gap of the free molecule is shifted into the valence band region of CoO, effectively suppressing the tunneling conductivity in that energy range.

5. Acknowledgements

This work was supported by the Deutsche Forschungsgemeinschaft (DFG) within the research unit “Functional Molecular Structures on Complex Oxide Surfaces (*funCOS*)” (project no. 214951840). M.A.S. gratefully acknowledges support and supply of CPU time by the Regionales Rechenzentrum Erlangen (RRZE).

References

- [1] W. Auwärter, D. Écija, F. Klappenberger, and J. V. Barth, *Nature Chemistry* **7**, 105 (2015).
- [2] J. M. Gottfried, *Surface Science Reports* **70**, 259 (2015).
- [3] H. Marbach, *Accounts of Chemical Research* **48**, 2649 (2015).

- [4] M. Lepper, J. Köbl, L. Zhang, M. Meusel, H. Hölzel, D. Lungerich, N. Jux, A. de Siervo, B. Meyer, H.-P. Steinrück, and H. Marbach, *Angewandte Chemie International Edition* **57**, 10074 (2018).
- [5] F. Gao, S. Song, X. Tang, H. Yi, S. Zhao, and Q. Yu, *Applied Surface Science* **506**, 144421 (2020).
- [6] B. O'Regan and M. Grätzel, *Nature* **353**, 737 (1991).
- [7] L. Ramoino, M. von Arx, S. Schintke, A. Baratoff, H.-J. Güntherodt, and T. Jung, *Chemical Physics Letters* **417**, 22 (2006).
- [8] S. H. Kim, H. Jeong, S. Lim, U. Ham, Y. Song, J. Yu, and Y. Kuk, *Surface Science* **613**, 54 (2013).
- [9] B. Sun, J. Li, W.-L. Dong, M.-L. Wu, and D. Wang, *The Journal of Physical Chemistry C* **120**, 14706 (2016).
- [10] F. Xiang, T. Schmitt, M. Raschmann, and M. A. Schneider, *Beilstein Journal of Nanotechnology* **11**, 1516 (2020).
- [11] G. Ashkenasy, A. Ivanisevic, R. Cohen, C. E. Felder, D. Cahen, A. B. Ellis, and A. Shanzer, *Journal of the American Chemical Society* **122**, 1116 (2000).
- [12] M. Lackinger, M. S. Janson, and W. Ho, *The Journal of Chemical Physics* **137**, 234707 (2012).
- [13] D. A. Cristaldi, A. Motta, S. Millesi, T. Gupta, M. Chhatwal, and A. Gulino, *J. Mater. Chem. C* **1**, 4979 (2013).
- [14] P. Rahe, M. Kittelmann, J. L. Neff, M. Nimmrich, M. Reichling, P. Maass, and A. Kühnle, *Advanced Materials* **25**, 3948 (2013).
- [15] S. Maier, L.-A. Fendt, L. Zimmerli, T. Glatzel, O. Pfeiffer, F. Diederich, and E. Meyer, *Small* **4**, 1115 (2008).
- [16] A. Amrous, F. Bocquet, L. Nony, F. Para, C. Lopacher, S. Lamare, F. Palmino, F. Cherioux, D. Z. Gao, F. F. Canova, M. B. Watkins, and A. L. Shluger, *Advanced Materials Interfaces* **1**, 1400414 (2014).
- [17] B. Hoff, M. Gingras, R. Peresutti, C. R. Henry, A. S. Foster, and C. Barth, *The Journal of Physical Chemistry C* **118**, 14569 (2014).
- [18] P. Olszowski, L. Zajac, S. Godlewski, B. Such, R. Jöhr, T. Glatzel, E. Meyer, and M. Szymonski, *The Journal of Physical Chemistry C* **119**, 21561 (2015).
- [19] A. Hinaut, R. Pawlak, E. Meyer, and T. Glatzel, *Beilstein Journal of Nanotechnology* **6**, 1927 (2015).
- [20] L. Lafför, F. A. Schlage, L. Kantorovich, P. J. Morarty, M. Reichling, and P. Rahe, *The Journal of Physical Chemistry C* **124**, 9900 (2020).
- [21] J. Schneider, F. Kollhoff, T. Schindler, S. Bichlmaier, J. Bernardi, T. Unruh, J. Libuda, T. Berger, and O. Diwald, *The Journal of Physical Chemistry C* **120**, 26879 (2016).
- [22] G. Di Filippo, A. Classen, R. Pöschel, and T. Fauster, *The Journal of Chemical Physics* **146**, 064702 (2017).
- [23] D. Wechsler, P. Vensaus, N. Tsud, H.-P. Steinrück, O. Lytken, and F. J. Williams, *The Journal of Physical Chemistry C* **125**, 6708 (2021).
- [24] C. Wang, R. Wang, J. Hauns, and T. Fauster, *The Journal of Physical Chemistry C* **124**, 14167 (2020).
- [25] T. Wähler, R. Schuster, and J. Libuda, *Chemistry – A European Journal* **26**, 12445 (2020).
- [26] J. van Elp, J. L. Wieland, H. Eskes, P. Kuiper, G. A. Sawatzky, F. M. F. de Groot, and T. S. Turner, *Physical Review B* **44**, 6090 (1991).
- [27] E. Z. Kurmaev, R. G. Wilks, A. Moewes, L. D. Finkelstein, S. N. Shamin, and J. Kuneš, *Physical Review B* **77**, 10.1103/physrevb.77.165127 (2008).
- [28] T. Xu, M. Schwarz, K. Werner, S. Mohr, M. Amende, and J. Libuda, *Chemistry – A European Journal* **22**, 5384 (2016).
- [29] M. Schwarz, C. Hohner, S. Mohr, and J. Libuda, *The Journal of Physical Chemistry C* **121**, 28317 (2017).
- [30] M. Schwarz, S. Mohr, C. Hohner, K. Werner, T. Xu, and J. Libuda, *The Journal of Physical Chemistry C* **123**, 7673 (2019).
- [31] M. Ammon, S. Baumann, T. Kißlinger, J. Rieger, T. Fauster, J. Redinger, L. Hammer, and M. A. Schneider, *physica status solidi (RRL) – Rapid Research Letters*, 2100383 (2021).
- [32] M. Lepper, T. Schmitt, M. Gurrath, M. Raschmann, L. Zhang, M. Stark, H. Hölzel, N. Jux, B. Meyer, M. A. Schneider, H.-P. Steinrück, and H. Marbach, *The Journal of Physical Chemistry C* **121**, 26361 (2017).
- [33] G. Kresse and J. Hafner, *Phys. Rev. B* **47**, 558 (1993).
- [34] G. Kresse and J. Furthmüller, *Comput. Mater. Sci.* **6**, 15 (1996).
- [35] G. Kresse and D. Joubert, *Phys. Rev. B* **59**, 1758 (1999).
- [36] J. P. Perdew, K. Burke, and M. Ernzerhof, *Phys. Rev. Lett.* **77**, 3865 (1996).
- [37] S. L. Dudarev, G. A. Botton, S. Y. Savrasov, C. J. Humphreys, and A. P. Sutton, *Phys. Rev. B* **57**, 1505 (1998).
- [38] K. Leung, I. M. B. Nielsen, N. Sai, C. Medforth, and J. A. Shelnut, *The Journal of Physical Chemistry A* **114**, 10174 (2010), PMID: 20726563, <https://doi.org/10.1021/jp1012335>.
- [39] A. Tkatchenko and M. Scheffler, *Phys. Rev. Lett.* **102**, 073005 (2009).
- [40] C. Tröppner, T. Schmitt, M. Reuschl, L. Hammer, M. A. Schneider, F. Mittendorfer, J. Redinger, R. Podlucky, and M. Weinert, *Phys. Rev. B* **86**, 235407 (2012).
- [41] K. Baraik, A. Bhakar, V. Srihari, I. Bhaumik, C. Mukherjee, M. Gupta, A. K. Yadav, P. Tiwari, D. M. Phase, S. N. Jha, S. D. Singh, and T. Ganguli, *RSC Adv.* **10**, 43497 (2020).
- [42] S. Otto and T. Fauster, *Journal of Physics: Condensed Matter* **28**, 055001 (2016).
- [43] L. Egger, M. Hollerer, C. S. Kern, H. Herrmann, P. Hurdax, A. Haags, X. Yang, A. Gottwald, M. Richter, S. Soubatch, F. S. Tautz, G. Koller, P. Puschnig, M. G. Ramsey, and M. Sterrer, *Angew. Chem. Int. Ed.* **60**, 5078 (2021).
- [44] C. Wang, Q. Fan, S. Hu, H. Ju, X. Feng, Y. Han, H. Pan, J. Zhu, and J. M. Gottfried, *Chemical Communications* **50**, 8291 (2014).
- [45] A. Wolfram, Q. Tariq, C. C. Fernández, M. Muth, M. Gurrath, D. Wechsler, M. Franke, F. J. Williams, H.-P. Steinrück, B. Meyer, and O. Lytken, *Surface Science* **717**, 121979 (2022).
- [46] J. Tersoff and D. R. Hamann, *Phys. Rev. B* **31**, 805 (1985).
- [47] A. Weber-Bargioni, W. Auwärter, F. Klappenberger, J. Reichert, S. Lefrançois, T. Strunskus, C. Wöll, A. Schiffrin, Y. Pennec, and J. V. Barth, *ChemPhysChem* **9**, 89 (2008).
- [48] J. Brede, M. Linares, R. Lensen, A. Rowan, M. Funk, M. Broering, G. Hoffmann, and R. Wiesendanger, *Journal of Vacuum Science & Technology B Microelectronics and Nanometer Structures* **27**, 799 (2009).
- [49] M. Lepper, J. Köbl, T. Schmitt, M. Gurrath, A. de Siervo, M. A. Schneider, H.-P. Steinrück,

- B. Meyer, H. Marbach, and W. Hieringer, *Chem. Commun.* **53**, 8207 (2017).
- [50] R. Adhikari, G. Sigleithmaier, M. Gurrath, M. Meusel, J. Kuliga, M. Lepper, H. Hölzel, N. Jux, B. Meyer, H.-P. Steinrück, and H. Marbach, *Chemistry – A European Journal* **26**, 13408 (2020).
- [51] O. Krejčí, P. Hapala, M. Ondráček, and P. Jelínek, *Physical Review B* **95**, 10.1103/physrevb.95.045407 (2017).
- [52] C. Weiss, C. Wagner, C. Kleimann, M. Rohlfing, F. S. Tautz, and R. Temirov, *Phys. Rev. Lett.* **105**, 086103 (2010).
- [53] S. Ditze, M. Stark, F. Buchner, A. Aichert, N. Jux, N. Luckas, A. Görling, W. Hieringer, J. Hornegger, H.-P. Steinrück, and H. Marbach, *Journal of the American Chemical Society* **136**, 1609 (2014), pMID: 24410182.
- [54] M. Stark, S. Ditze, M. Lepper, L. Zhang, H. Schlott, F. Buchner, M. Röckert, M. Chen, O. Lytken, H.-P. Steinrück, and H. Marbach, *Chem. Commun.* **50**, 10225 (2014).
- [55] W. Auwärter, K. Seufert, F. Bischoff, D. Ecija, S. Vijayaraghavan, S. Joshi, F. Klappenberger, N. Samudrala, and J. V. Barth, *Nature Nanotechnology* **7**, 41 (2011).
- [56] K. Diller, A. C. Papageorgiou, F. Klappenberger, F. Allegretti, J. V. Barth, and W. Auwärter, *Chem. Soc. Rev.* **45**, 1629 (2016).
- [57] H. Marbach and H.-P. Steinrück, *Chemical Communications* **50**, 9034 (2014).
- [58] D. Wechsler, C. C. Fernández, Q. Tariq, N. Tsud, K. C. Prince, F. J. Williams, H.-P. Steinrück, and O. Lytken, *Chemistry – A European Journal* **25**, 13197 (2019).
- [59] A. C. Papageorgiou, S. Fischer, S. C. Oh, O. Sağlam, J. Reichert, A. Wiengarten, K. Seufert, S. Vijayaraghavan, D. Écija, W. Auwärter, F. Allegretti, R. G. Acres, K. C. Prince, K. Diller, F. Klappenberger, and J. V. Barth, *ACS Nano* **7**, 4520 (2013).
- [60] J. I. Urgel, M. Schwarz, M. Garnica, D. Stassen, D. Bonifazi, D. Ecija, J. V. Barth, and W. Auwärter, *Journal of the American Chemical Society* **137**, 2420 (2015).
- [61] F. Bischoff, K. Seufert, W. Auwärter, A. P. Seitsonen, D. Heim, and J. V. Barth, *The Journal of Physical Chemistry C* **122**, 5083 (2018).
- [62] B. D. Baker Cortés, N. Schmidt, M. Enache, and M. Stöhr, *The Journal of Physical Chemistry C* **123**, 19681 (2019).
- [63] J. Kuliga, R. C. de Campos Ferreira, R. Adhikari, S. Massicot, M. Lepper, H. Hölzel, N. Jux, H. Marbach, A. de Siervo, and H.-P. Steinrück, *ChemPhysChem* **22**, 396 (2021).
- [64] T. Yokoyama, S. Yokoyama, T. Kamikado, Y. Okuno, and S. Mashiko, *Nature* **413**, 619 (2001).
- [65] X. Lin, N. Nilius, H.-J. Freund, M. Walter, P. Frondelius, K. Honkala, and H. Häkkinen, *Phys. Rev. Lett.* **102**, 206801 (2009).
- [66] J. Pal, M. Smerieri, E. Celasco, L. Savio, L. Vattuone, and M. Rocca, *Phys. Rev. Lett.* **112**, 126102 (2014).
- [67] P. Hurdax, M. Hollerer, P. Puschnig, D. Lüftner, L. Egger, M. G. Ramsey, and M. Sterrer, *Advanced Materials Interfaces* **7**, 2000592 (2020).
- [68] J. Repp, G. Meyer, S. M. Stojković, A. Gourdon, and C. Joachim, *Physical Review Letters* **94**, 026803 (2005).
- [69] P. Liljeroth, J. Repp, and G. Meyer, *Science* **317**, 1203 (2007).
- [70] S. Wang, L. Talirz, C. A. Pignedoli, X. Feng, K. Müllen, R. Fasel, and P. Ruffieux, *Nature Communications* **7**, 10.1038/ncomms11507 (2016).